Modeling of whole-space transient electromagnetic responses based on FDTD and its application in the mining industry

Jingcun Yu, Reza Malekian, *Member, IEEE*, Jianghao Chang, Benyu Su

***Abstract*—Hidden, water-abundant areas in coal mines pose a serious threat to mine safety and production. Underground transient electromagnetic method (TEM) is one of the most effective means of detecting water-abundant areas in front of the roadway head. Traditional TEM theories and applications are interpreted mainly on the vertical component. In this study, multi-component responses of TEM in underground roadways were modeled using the finite-difference time-domain (FDTD) method. Physical simulation was also used for advanced detection of TEM in the roadway. Both the numerical and physical simulation results show that the horizontal component is more sensitive to the location of water-abundant areas. The results of the joint interpretation with both horizontal and vertical components were verified in a practical coal mine application, indicating that it is feasible to use the horizontal component in interpreting TEM data. Thus, the horizontal component could serve as a new approach for coal mine TEM data processing and interpretation.**

This work was supported in part by the State Key Research Development Program of China (NO. 2017YFC0804401), in part by the China Postdoctoral Science Foundation (NO.110101/3445), and in part by the National Research Foundation, South Africa (RDYR160404161474). *(Corresponding author: Jianghao Chang.)*

Jingcun Yu is with the School of Resources and Geosciences, China University of Mining and Technology, Xuzhou, 221116, China (e-mail: yujcun@163.com).

Reza Malekian is with the Department of Electrical, Electronic and Computer Engineering, University of Pretoria, Pretoria, 0002, South Africa (e-mail: reza.malekian@ieee.org).

Jianghao Chang is with the School of Exploration Technology and Engineering, Hebei GEO University, Shijiazhuang, 050031, China (e-mail: jhchang@126.com).

Benyu Su is with the School of Resources and Geosciences, China University of Mining and Technology, Xuzhou, 221116, China (e-mail: subenyu@cumt.edu.cn).

***Index Terms*—Transient electromagnetic method, Coal mine industry, Advanced detection, Numerical modeling, finite-difference time-domain (FDTD)**

I. INTRODUCTION

Water disasters are a serious threat to coal mine safety and production, and underground driving roadways are the most common locations where water inrush occurs [1]. Water inrush can result in severe economic losses and casualties. To ensure safe mining, in [2] a complete mine safety system using a wireless sensor network was developed. Mine water generally has the characteristics of high mineralization and low resistivity, thus the resistivity of water-bearing structures in mines are lower than that of normal formations. As a result of this, geophysical methods are used to detect water-bearing structures in the mines. In [3-4] the electrical anisotropic response of water conducted fractured zone of the mining goaf was studied. With an increase in the mining depth, underground detection has more advantages than the ground. Transient electromagnetic method (TEM), which has the advantages of high sensitivity to low-resistance bodies and can be easily constructed [5-9], is one of the primary methods for detecting water-bearing structures down in the mines.

The transmission and reception of traditional TEM is carried out on the ground, and the detected geological anomalies are all located under the ground; its measurement signals are mainly vertical components. In this paper, TEM is used to detect hidden water-abundant areas in coal mines. When transmission and reception are conducted in the underground roadway of the coal mine, the targeted body can be located in the roadway floor strata, in front of the roadway or in the roof strata, thus increasing the difficulty of the data interpretation. To solve these problems, in this paper, the multi-component responses of whole-space TEM were studied. We found that the horizontal component was more sensitive to the position of the anomalous body. Thus, the joint interpretation of the vertical and horizontal components can locate the water-abundant areas more accurately.

Against the above background, the contributions of this paper can be summarized as follows: 1) The finite-difference time-domain (FDTD) numerical simulation and physical simulation methods were used to simulate the vertical and horizontal component responses of the whole-space TEM. The results obtained from the two methods were basically consistent, indicating that the horizontal component is indeed more sensitive to the position of anomalous bodies underground the coal mine. 2) Joint interpretation of the vertical and horizontal components were proposed by analyzing the law of multi-component responses, which could result in accurately locating water-abundant areas underground the coal mine.

The FDTD method is one of the main methods used in the numerical modeling of electromagnetic fields [10]. In order to realize the numerical modeling of the transient electromagnetic field by FDTD, [11] modified the magnetic field curvature equation under quasi-static conditions. Currently, studies on TEM theories and applications are mainly based on the vertical magnetic-field component in half-space, and TEM dataprocessing and inversion are only based on the vertical component [12-13]. However, the horizontal component can also reflect some information on anomalous bodies, and joint interpretation with both the horizontal and vertical components can improve the precision of data interpretation. Some new techniques can also be applied to signal extraction and inversion of multi-component in the future [14-15]. In the multi-component study of TEM, [16] calculated the responses of both the vertical and the horizontal components from a conductive plate in half-space, and analyzed the different components' abilities of reflecting the anomalous body. Using the finite-difference time-domain (FDTD) method, in [17] the vertical component and horizontal component responses of a three-dimensional (3-D) conductor at a fault contact in half space was studied. In [18], numerical modeling and physical experiments on transient electromagnetic multi-component responses with the aim of unexploded ordnance detection was carried out. By replacing the eddy current with eigencurrent, [19] calculated the responses of three directions from the thin plate conductor in half- space with various dip angles. All the above studies were carried out in half-space; however, responses of TEM down the coal mines are whole-space responses, and would be influenced by the whole space. Thus, the multi-component responses of whole-space TEM in coal mines is studied here.

Both the transmission and reception of TEM down in the coal mine were performed in an underground roadway, thus only small loop devices with a length of less than 3 m could be used. Small loop devices can be readily rotated, and are convenient for receiving components in various directions. Multi-component responses of goaf water ahead of the roadway head in coal mines were numerically modeled by using the 3-D FDTD. The simulation results, together with the experimental results were then used to derive the characteristics of the multi-component responses and further propose the multi-component interpreting method for mine transient electromagnetic method (MTEM). Practical applications in underground detection showed that the horizontal component could serve as a new approach to underground TEM data processing and interpretation.

II. FDTD FOR TRANSIENT ELECTROMAGNETIC FIELD

A. Governing equations

In isotropic media, Maxwell's equations can be written as [10]:

$$\nabla \times E = -\frac{\partial B}{\partial t}, \quad (1)$$

$$\nabla \times H = J + \frac{\partial D}{\partial t}, \quad (2)$$

$$B = \mu H, \quad (3)$$

$$D = \varepsilon E, \quad (4)$$

Where, E is the electric field intensity, B is the magnetic induction intensity, H is the magnetic field intensity, D is the electric displacement vector, μ is the permeability, and ε is the permittivity. In [10] the FDTD method for electromagnetic field calculation was developed, and used the grid as shown in Fig 1. In the Yee grid, the magnetic-field components are placed in the center of the faces, and the electric-field components are placed in the middle of the edges. This pattern can guarantee that continuity conditions of the field components on the discontinuous surface are naturally met, which is convenient for computing complex structures.

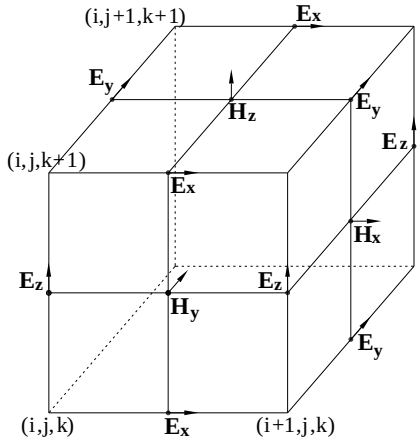

Fig. 1 Positions of the field components in the Yee grid [10].

When directly using the 3-D difference scheme (Equation (1) and Equation (2)) to iterate, the following stability condition should be met [10].

$$\Delta t \le \Delta_{\min} \sqrt{\frac{\mu\varepsilon}{3}}, \quad (5)$$

Where, $\Delta_{\min}$ is the minimum grid spacing, ε is the vacuum permittivity and μ is the vacuum permeability. Assuming the grid is a 1 m^3 cube, the maximum time step is 1.9254×10^{-9} s, and it needs at least 519378 iterations to compute the responses in the time domain of 1 ms. This would consume a lot of time and could hardly be achieved on ordinary computers.

The working frequency of TEM is generally below 10^6 Hz; for the ground medium, the displacement current is much smaller than the conduction current, so the displacement current can be ignored, that is, quasi-static approximation is performed. Under quasi-static conditions, Maxwell's equations in source-free, lossy, nonmagnetic media can be written as [20]:

$$-\frac{\partial B}{\partial t} = \nabla \times E, \quad (6)$$

$$\sigma E = \nabla \times H, \quad (7)$$

$$\nabla \bullet B = 0, \quad (8)$$

$$\nabla \bullet E = 0, \quad (9)$$

Where, σ is the conductivity of the medium, J is the conduction current density. Because displacement current is ignored, Equation (7) does not contain the time derivative term of the electric field, and the explicit scheme required by FDTD cannot be formed. For the needs of FDTD calculation, [11] turned Equation (7) to :

$$\gamma \frac{\partial E}{\partial t} + \sigma E = \nabla \times H, \quad (10)$$

Where, the first term on the left is the fictitious displacement current, which allows a large time step in computing late-time electromagnetic field and the calculation accuracy is unaffected.

After introducing the fictitious displacement current, the explicit difference scheme of Equation (10) can be written as [11]:

$$\gamma \frac{\partial E_x}{\partial t} + \sigma E_x = \frac{\partial H_z}{\partial y} - \frac{\partial H_y}{\partial z}, (11)$$

$$\gamma \frac{\partial E_y}{\partial t} + \sigma E_y = \frac{\partial H_x}{\partial z} - \frac{\partial H_z}{\partial x}, (12)$$

$$\gamma \frac{\partial E_z}{\partial t} + \sigma E_z = \frac{\partial H_y}{\partial x} - \frac{\partial H_x}{\partial y}. (13)$$

Equation (8) indicates that only two of the three components of the magnetic induction intensity are independent. In numerical calculations of the electromagnetic fields, electromagnetic fields in the late time are mainly low-frequency fields. Thus the explicit expression of Equation (8) has to be included in the iteration, or else the results would be incorrect. When computing magnetic fields, [11] first calculated the two magnetic-field components by using Equation (6), and then calculated the other components using Equation (8). The specific equations are as follows [11]:

$$-\frac{\partial B_x}{\partial t} = \frac{\partial E_z}{\partial y} - \frac{\partial E_y}{\partial z}, (14)$$

$$-\frac{\partial B_y}{\partial t} = \frac{\partial E_x}{\partial z} - \frac{\partial E_z}{\partial x}, (15)$$

$$\frac{\partial B_z}{\partial z} = -\frac{\partial B_x}{\partial x} - \frac{\partial B_y}{\partial y}. (16)$$

B_z value of a layer of grid units needs to be known when applying Equation (16). In [11] the B_z value of the bottom boundary layer was set as 0, thereafter the B_z values of all the layers from the bottom to top were calculated. Equation (6) was first used in [9] to calculate the B_z value of the middle layer (z=0) in whole-space, and then calculated B_z values of the layers up and down (as shown in Fig. 2).

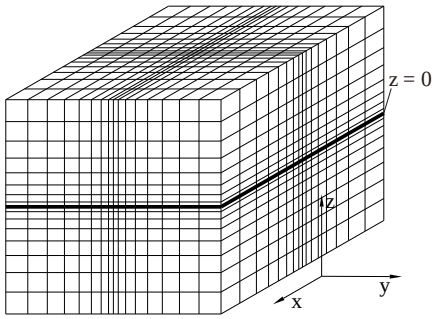

Fig. 2 Diagram of the discretization for the three-dimensional whole-space model.

The equations above are only applicable for a source-free region, and the following equation should be applied for electric fields in the region where the source is located [21]:

$$\gamma \frac{\partial E}{\partial t} + \sigma E + J_s = \nabla \times H, \quad (17)$$

Where, J_s is the source current density. By using the difference method to Equation (17), the difference equations for the electric fields in the source region can be obtained [21]. The calculation method for the magnetic fields in the source region is the same as that for the magnetic fields in the source-free region.

B. Boundary conditions

Appropriate boundary conditions should be applied to the 6 truncating boundaries of the whole-space model. Convolutional perfectly matched layer (CPML) not only has the features of PML absorbing boundary, but can also effectively absorb low-frequency fields [22-23]. The CPML boundary conditions were used in this study to solve the whole-space transient electromagnetic problem.

C. Verification of the Method

In this study, the difference equations under quasi-static conditions are used for numerical simulation. In

order to verify the reliability of the method, the quasi-static results are compared with the results of the direct Yee algorithm, Fig. 3 shows the comparative result of the induced electromotive force. Both the transmitting and receiving loops are 2 m × 2 m and the transmitting waveform is a trapezoidal wave. It can be seen from Fig. 3 that the results under quasi-static condition agree with the results of the direct Yee algorithm, which shows that the quasi-static handling method combined with fictitious displacement current can calculation time and more importantly, the accuracy of the solution is not affected.

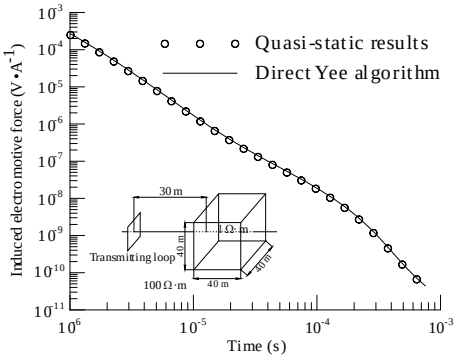

Fig. 3 Comparison of the quasi-static result and the result of the direct Yee algorithm for the whole-space model.

III. RESULTS OF NUMERICAL MODELING

A. Horizontal component responses of goaf water right ahead of the roadway head

Water in goaf is a common source of water inrush in the underground driving roadway. By taking the water-filled goaf as an example, multi-component responses in whole-space were studied using TEM. Based on the geological data of the coal-bearing strata in various mining areas, a 3-D whole-space model of the coal-bearing strata was established. In the model, roof resistivity and floor resistivity were set as 100 Ω·m and 150 Ω·m, respectiveely. Resistivity of coal seam was set as 400 Ω·m, and the thickness of the coal seam was set at 10 m, as shown in Fig. 4. The underground observation mode for the components is shown in Fig. 5. The transmitting and receiving loops were located at the underground roadway head. The number of turns of the transmitting loop was 40, and that of the receiving loop was 60. Both horizontal and vertical components were observed and measured while transmitting. The receiving loop coinciding with the

transmitting loop would receive the vertical component, while the receiving loop perpendicular with the transmitting loop would receive the horizontal component.

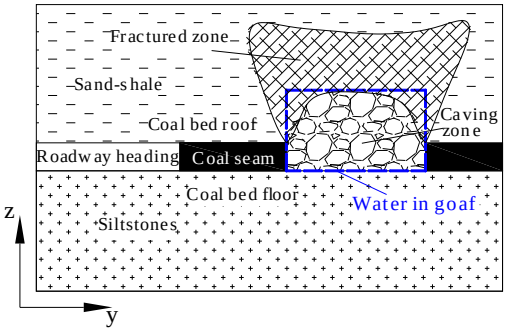

Fig. 4 Profile of water in goaf.

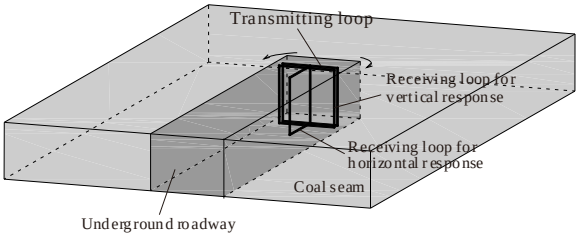

Fig. 5 Multi-component observation mode.

A 3-D low-resistance body, which was used to represent the water-filled goaf, was set right ahead of the roadway head. The length of each side of the low-resistance body was 30 m, and its resistivity was set as 0.5 Ω·m. The plan view of the model is shown in Fig. 6. Measuring points around the roadway head were arranged at various angles and in the manner of a sector, and the transmitting loop and receiving loops were rotated simultaneously. Transmission directions are shown in Fig. 6, in which the indicated direction is normal to the transmitting loop. The transmitting waveform is a trapezoidal wave. The duration of the trapezoidal wave is 8 ms and the rising and falling edges are 1 μs. The time step in the rising and falling edges is 1ns, at other times the time step gradually increased.

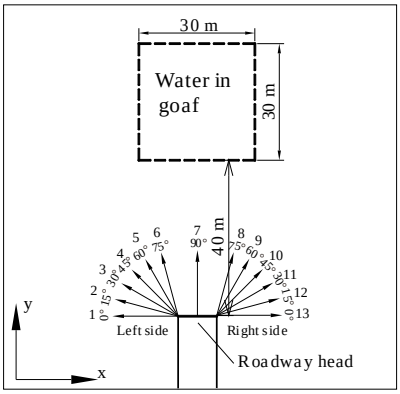

Fig. 6 Model of goaf water right ahead of the roadway head and the transmitting directions.

Fig. 7 shows the response curves of the horizontal component obtained through forward modeling at left side 45° (measuring point No. 4), left side 60° (measuring point No. 5), and left side 75° (measuring point No. 6), respectively. In the figure, the vertical coordinate represents normalized induced electromotive force; the solid line represents positive value, while the dotted line represents negative value. As can be seen from the figure, the response curves corresponding to different detection angles have the same pattern; namely, the induced electromotive force in all three cases was negative at the beginning, then turned positive, and after a while, changed back to negative and decreased with time. However, the response amplitude varied obviously among the different detection directions; the maximum amplitude was observed at left side 45°, and the minimum amplitude was observed at left side 75°. The reason for this difference is that horizontal component reflects the degree of asymmetry of the media on left and right sides of the transmitting loop. When the detection direction was at 90° (measuring point No. 7), the media on left and right sides of the transmitting loop were perfectly symmetrical and the horizontal component was 0.

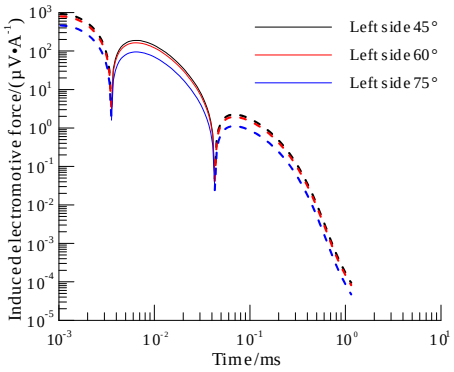

Fig. 7 Response curves of the horizontal component at different detection angles.

Fig. 8 shows the multi-channel profiles obtained through forward modeling, and Fig. 8a and Fig. 8b show the results of the vertical and horizontal component respectively. In the figures, the horizontal coordinate represents measuring points, and the vertical coordinate represents normalized induced electromotive force. The thirteen measuring points correspond to the detection directions of left side 0°, left side 15°, and right side 0° successively. In Fig. 8a, all the profile curves at different times indicate single-peak anomalies, with the strongest anomalous response occurring at measuring point No. 7 (at 90°), which was located right ahead of the roadway head. Fig. 8b shows that the horizontal component was negative at left side angles, while the component was positive at right side angles. The negative maximum and positive maximum were observed at measuring point No. 4 and No. 10, respectively and the response was 0 at the point right ahead of the roadway head (i.e. measuring point No. 7 in Fig. 8b). The reason for the 0 point is that, when the transmitting direction was along the roadway, the media on both sides of the transmitting loop were perfectly symmetrical and their horizontal responses cancelled each other out. With the transmitting direction changing from 90° to the right side angles, the horizontal component increased gradually, reaching to the maximum at measuring point No. 10 (right side 45°), and then decreased gradually. As can be seen from Fig. 8b, responses at left side and right side were opposite in sign but identical in amplitude. The results of the vertical component and the horizontal component, as shown in Fig. 8, indicate that the horizontal component was more sensitive to the location of the anomalous body and thus is better for determining the direction of anomalous bodies.

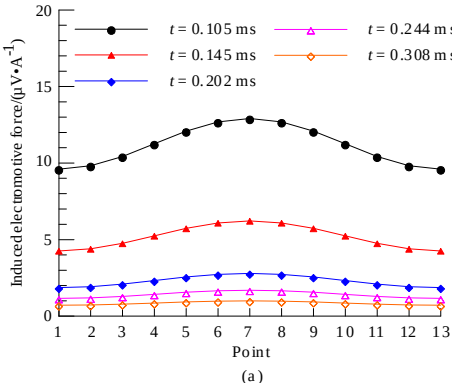

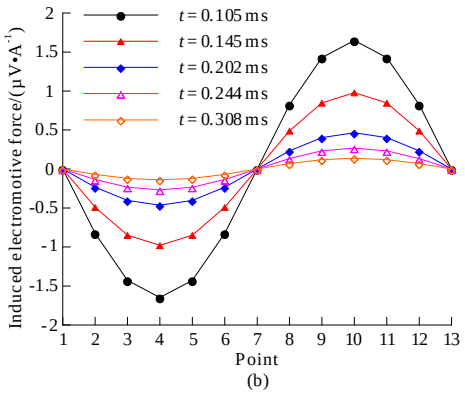

Fig. 8 Multi-channel profiles for the anomalous body right ahead of roadway head.

(a) Vertical component (b) Horizontal component

B. Horizontal component responses of goaf water on one side of the roadway head

In actual underground detection, the water-bearing area may exist anywhere in front of the roadway head. Responses of goaf water on the right side of the roadway head were calculated in this study. Fig. 9 shows the plan view of the model.

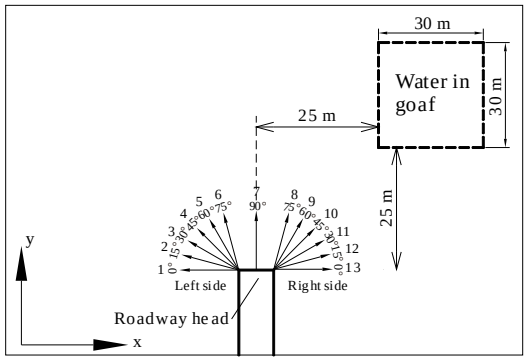

Fig. 9 Model of goaf water on the right side of the roadway head.

Fig. 10 shows the multi-channel profiles obtained through forward modeling of the model shown in Fig. 9, and Fig. 10a and Fig.10b show the results of vertical component and horizontal component respectively. In Fig. 10a, the maximum of all the profile curves at different times occurred at measuring point No. 10 (right side 45°), indicating the orientation of the goaf water correctly. In Fig. 10b, each of the horizontal component curves has two zero points, which correspond to the measuring point No. 4 (left side 45°) and No. 10 (right side 45°) respectively. The detection direction at the measuring point No. 10 was identical to the direction of the goaf water; when detecting at this angle, the media on both sides of the transmitting loop were perfectly

symmetrical and the horizontal component of the responses was 0. At measuring point No. 4, the curves in Fig. 10a reaches the lowest and the transmitting direction was completely orthogonal to the direction of the goaf water; the influence of the anomalous body on the responses was minimal, and thus both the vertical and horizontal components were weak. By comparing Fig. 10b with Fig. 8b, it can be seen that changes in the pattern of the curves are consistent with changes in the location of the anomalous body, thus the horizontal component can serve as a new means of locating anomalous bodies.

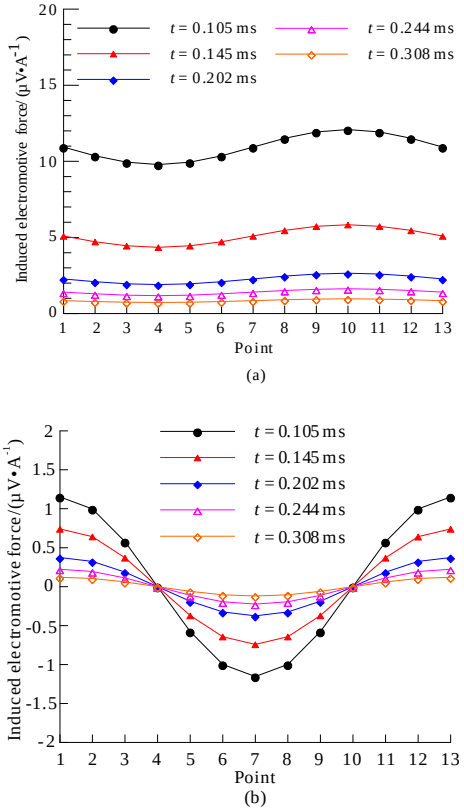

Fig. 10 Multi-channel profiles for the anomalous body on the right-front side of the roadway head.

(a) Vertical component (b) Horizontal component

IV. SIMILARITY CRITERIA FOR PHYSICAL SIMULATION

Physical simulation is important in TEM studies, and the results from physical simulation can be used to verify numerical modeling results. Physical simulation refers to the method of using a scale model in the laboratory to simulate a field system. The similarity criteria for physical simulation in the time-domain electromagnetic method are as follows [24]:

$$\frac{\sigma_1 n^2}{t_1} = \frac{\sigma m^2}{t}, \quad (18)$$

$$\frac{\sigma_1}{t_1} = \frac{P^2 \sigma}{t}, \quad (19)$$

Where, σ_1 and σ are the conductivity of the model system and field system respectively, m and n are the characteristic length (or linearity) of the field system and model system respectively, t_1 and t are the time parameters of the model system and field system respectively, and $P = m/n$ is the scale factor.

In TEM, the observed secondary induced voltage, $V(t)$, is in proportion to the transmitting current, I, linear scale of the system, and $1/t$, thus it is necessary to include the condition defining the relation between the observed voltage of the two systems. Assume that the transmitting loop in the model system is a square loop, whose side length and number of turns are L_1 and N_{T1} respectively. The receiving loops in the model system are square loops, whose side length and number of turns are l_1 and N_{R1} respectively. The transmitting loop in the field system is a square loop, whose side length and number of turns are L and N_T respectively. The receiving loops in the field system are square loops, whose side length and number of turns are l and N_R respectively. We then obtain the following as in [24]:

$$\frac{V_1(t)/I_1}{V(t)/I} = \frac{L_1^2 N_{T1} N_{R1}}{L^2 N_T N_R} \cdot \frac{t l^2}{t_1 l_1^2}. \quad (20)$$

Equation (20) is the required additional criterion. Through this equation, the proportional factors between the observed data of the two systems can be obtained.

V. RESULTS OF PHYSICAL SIMULATION

The Terra TEM instrument (Australia) was used for the experiment. Both the transmitting and receiving loops were square loops with side lengths 10 cm. The number of turns of the transmitting loop was 40, and that of the receiving loop was 60. Air was used as the whole-space uniform medium, and a copper rod, which was 30 cm in length and 10 cm in diameter, was used as the anomalous body. The scale factor was 100. The physical models are shown in Fig. 11. The anomalous body was located right ahead of the roadway head,

corresponding to the anomalous body 1 in Fig. 11a; the anomalous body was located on the right side of the roadway head, corresponding to the anomalous body 2 in Fig. 11b. In the simulation, the sectorial manner at an interval of 15° from left to right was used to detect the anomalous body, and the observation mode was same as the mode shown in Fig. 5.

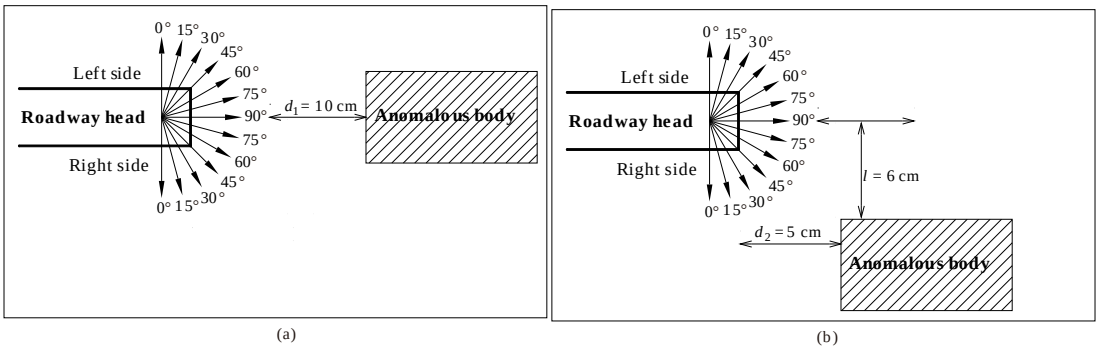

Fig. 11 Diagram of the physical models.

Fig. 12 shows the results from the simulation of model in Fig. 11a. The 13 measuring points correspond to the 13 detection directions shown in Fig. 11a, respectively. In Fig. 12a, the vertical component reached the maximum at measuring point No. 7, where the detection direction pointed to the central position of the anomalous body, indicating a low-resistance anomalous response. In Fig. 12b, the horizontal component reached 0 at the measuring point No. 7 (90°). The reason for the 0 point is that the media on the left and right sides of the transmitting loop were perfectly symmetrical about the detection direction and their horizontal responses cancelled each other out. This is consistent with the numerical modeling results. The minimum and maximum peak values were observed respectively at measuring point No. 5 and No. 9. When the detection direction turned further to the left side and right side, the amplitude of the horizontal component increased somewhat, and reached the maximum at the left side 0° and the right side 0°. The horizontal component became bigger at 0° and 15° on both the left and right sides because one side of the transmitting loop got closer to the anomalous body when detecting the side areas in the physical simulation.

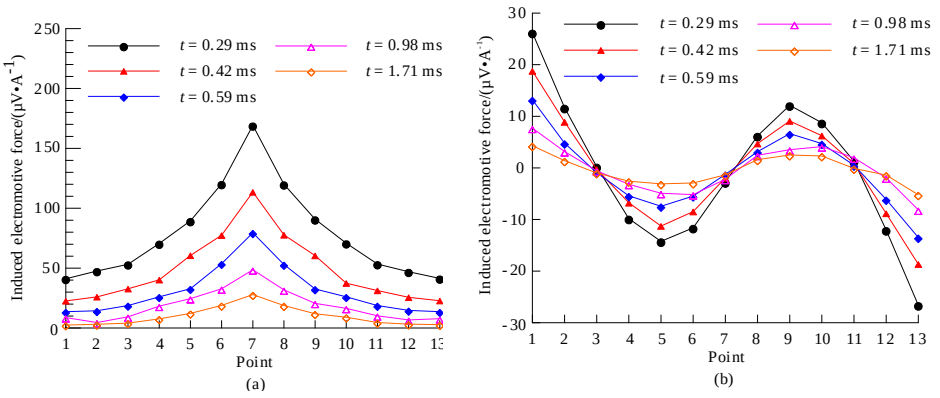

Fig. 12 Results from the physical simulation of the right-ahead anomalous body.

(a) Vertical component (b) Horizontal component

Fig. 13 shows the results from the simulation of the model in Fig. 11b. In Fig. 13a, the vertical component was higher when detecting on the right side, indicating a low-resistance anomalous response, and this is consistent with the numerical modeling results. In Fig. 13b, the horizontal component reached 0 between the measuring point No. 9 and No. 10, correctly indicating the position of the anomalous body, and this is consistent with the numerical modeling results. It can be concluded from the above numerical modeling and physical simulation that the horizontal component was more sensitive to the location of the anomalous body and can serve as a new means of locating anomalous bodies. Also, the joint interpretation with both the horizontal and the vertical components would be better for determining the direction of anomalous bodies.

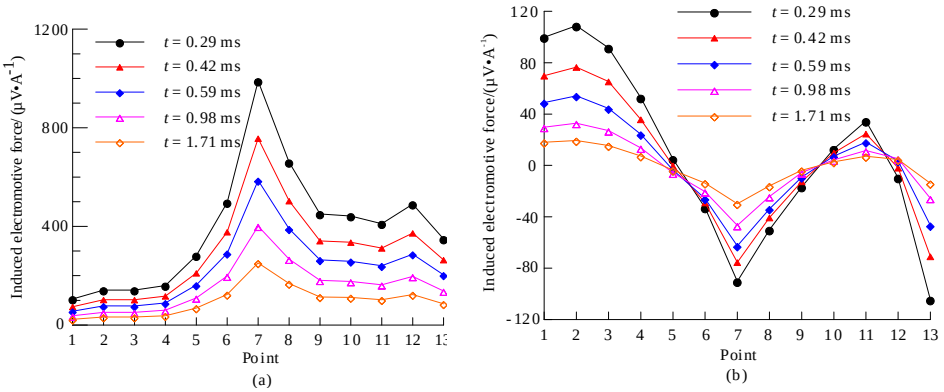

Fig. 13 Results from the physical simulation of the anomalous body on the right-front side.

(a) Vertical component (b) Horizontal component

VI. PRACTICAL APPLICATION

To verify the actual effect of the multi-component interpretation in interpreting the underground TEM data, multi-component advanced detection experiments were carried out in the head entry of the 103 panel of a coal mine in Huaibei, China. The exposed formations of the mine (partially) include a quaternary system, an Oligocene system, and a Shanxi formation of Permian system from top to bottom. An Archaean era limestone aquifer underlies the bottom of the shaft. The formation is 133.88 m in total thickness and contains 13 layers of limestone with a thickness of 71.10 m, accounting for 53% of the Taiyuan formation. A single layer of limestone is about 0.60~15.88 m in thickness, and the third, fourth, fifth, and thirteenth layers are thicker. Water in the mine is mainly fracture water, and the hydro geological condition belongs to the medium type. Fig. 14 shows the plan of the head entry of the 103 panel. Advanced detection was carried out in the roadway head to find out the water enrichment situation in the formation ahead. The Terra TEM instrument and 2 m × 2 m small multi-turn loops were used.

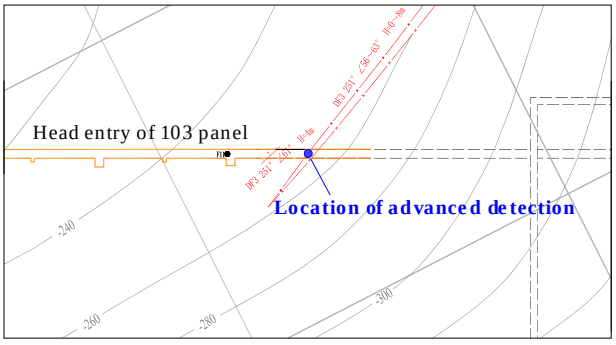

Fig. 14 Plan of the head entry of the 103 panel in a coal mine.

Fig. 15 shows the TEM multi-component advanced detection results. As can be seen from Fig. 15a, there are three maximum peak values of the vertical component on the profile of the transient electromagnetic induced potential, which are 441 μV/A at measuring point No. 3,965 μV/A at measuring point No.6, and 2,491 μV/A at measuring point No. 8. Of the three maximum peak values, the largest one was observed at measuring point No. 8, where the detection direction pointed to the anomalous point. It can be seen from Fig. 15b that there are three zero crossing points (ZCP) of the horizontal component of the transient

electromagnetic induced potential, which correspond to measuring point No. 2, measuring point No. 8, and measuring point No.11, respectively. There are a maximum and minimum value on both sides of the measuring point No. 8. The maximum value of 177 μV/A corresponds to measuring point No. 6, and the minimum value of 157 μV/A corresponds to measuring point No. 10. In addition, the range of positive values on the left side of measuring point No. 8 is greater than the range of negative values on the right side, presenting a left-right asymmetry.

Through comprehensive analysis of Fig. 15a and Fig. 15b, it can be concluded that the vertical component indicated the low-resistance body in the form of peak value anomaly, while the horizontal component indicated the low-resistance body in the form of ZCP anomaly. The horizontal component changed dramatically on the right side of measuring point No. 8, indicating that the anomalous body was located on the right side; the horizontal component was also more sensitive to the location of the anomalous body than the vertical component. Combining the horizontal component and vertical component results together can result in identifying the location of anomalous bodies more accurately. By combining the above detection results with hydro geological data, the comprehensive analysis indicated that there was a water-filled fractured zone on the right-front side of the roadway, and the central position of the fractured zone was located at about 15° on the right side of the roadway head and inclined to the right. Personnel related to the coal mine tested the prediction through drilling, and proved that the indicated place was indeed a water-abundant area. Therefore, the results of the TEM multi-component detection were verified.

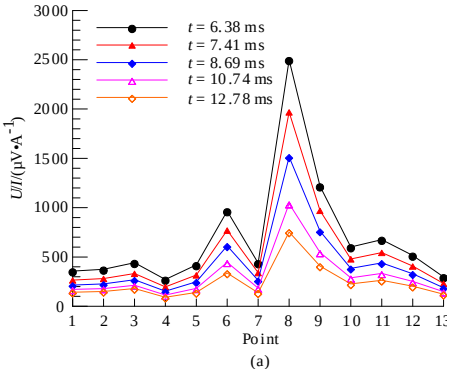

(a)

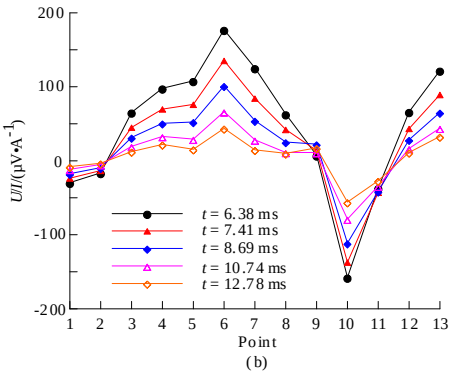

Fig. 15 Profile of the measured induced potential in a mine.

(a) Vertical component (b) Horizontal component

VII. CONCLUSIONS

Using the 3-D FDTD method, whole-space multi-component TEM responses were numerically modeled. Physical simulation was carried out based on the sectorial arrangement of measuring points for transient electromagnetic advanced detection, and the following characteristics of the whole-space multi-component TEM responses were obtained:

(1) The vertical component reflects the amplitude of the anomalous responses, while the horizontal component mainly reflects the asymmetry between the media on the left and right sides and thus is more sensitive to the location of anomalous bodies.

(2) The joint interpretation method of the vertical component and horizontal component was proposed by analyzing the law of the multi-component responses. Practical coalmine application indicated that comprehensive analysis of both the horizontal and vertical component could result in more accurate location and range identification of water-rich areas. The horizontal component could serve as a new approach to coalmine TEM data processing and interpretation.

REFERENCES

[1] Q. Wu, Y. Liu, L. Luo, et al., "Quantitative evaluation and prediction of water inrush vulnerability from aquifers overlying coal seams in Donghuantuo Coal Mine, China". Environmental Earth Sciences, vol.74, no.2, pp.1429-1437, 2015.

[2] V. Henriques, R. Malekian, "Mine Safety System Using Wireless Sensor Network", IEEE Access, Vol.4, pp. 3511-3521, 2016.

[3] B. Su, R. Malekian, J. Yu, et al., "Electrical Anisotropic Response of Water Conducted Fractured Zone in the Mining Goaf", IEEE Access, Vol.4, pp.6216-6224, 2016.

[4] B. Su, J. Yue. "Research of the electrical anisotropic characteristics of water-conducting fractured zones in coal seams". Applied Geophysics, vol.14, no.2, pp. 216-224, 2017.

[5] M. Commer, G Hoversten, E. Um. "Transient-electromagnetic finite-difference time-domain earth modeling over steel infrastructure". Geophysics, vol.80, no.2, pp. E147-E162, 2015.

[6] N. Zhou, G. Xue, W. Chen, et al., "Large-depth hydrogeological detection in the North China-type coalfield through short-offset grounded-wire TEM". Environmental Earth Sciences, vol.74, no.3, pp.2393-2404, 2015.

[7] J. C. Yu, Z. X. Liu, and S. C. Liu, et al., "Theoretical analysis of mine transient electromagnetic method and its application in detecting water burst structures in deep coal stope". Journal of the China Coal Society, vol.32, no.8, pp.818–821, 2007.

[8] J. L. Cheng, F. Li, S. P. Peng, et al., "Joint inversion of TEM and DC in roadway advanced detection based on particle swarm optimization". Journal of Applied Geophysics, vol.123, pp.30-35, 2015.

[9] J. H. Chang, J. C. Yu, and Z. X. Liu, "Three-dimensional numerical modeling of full-space transient electromagnetic responses of water in goaf". Applied Geophysics, vol.13, no.3, pp.539-552, 2016.

[10] K. S. Yee, "Numerical solution of initial boundary value problems involving Maxwell’s equations in isotropic media". IEEE Trans. Antennas Propag, vol.14, no.3, pp.302-307, 1966.

[11] T. Wang, G. W. Hohmann, "A finite-difference, time-domain solution for three-dimensional electromagnetic modeling". Geophysics, vol.58, no.6, pp.797-809, 1993.

[12] J. E. Danielsen, E. Auken, F. Jørgensen, et al., "The application of the transient electromagnetic method in hydrogeophysical surveys". Journal of Applied Geophysics, vol.53, no.4, pp.181-198, 2003.

[13] G. Q. Xue, X. Li, L. J. Gelius, et al., "A new apparent resistivity formula for in-loop fast sounding TEM theory and application". Journal of Environmental and Engineering Geophysics, vol.20, no.2, pp.107-118, 2015.

[14] X. Jin • J. Shao • X. Zhang, et al., "Modeling of nonlinear system based on deep learning framework", Nonlinear Dynamics, Springer, Vol.84, No. 3, pp.1327-1340, 2016.

[15] Z. Xin, S. Jie, A. Wenwei,Y. Tiantian, et al., "An Improved Time-Frequency Representation based on Nonlinear Mode Decomposition and Adaptive Optimal Kernel", Elektronika ir Elektrotechnika, Vol. 22, No.4, pp.52-57, 2016.

[16] J. D. McNeill, R. N. Edwards, G. M. Levy, "Approximate calculations of the transient electromagnetic response from buried conductors in a conductive half-space". Geophysics, vol.49, no.7, pp.918-924, 1984.

[17] T. Wang, A. C. Tripp, G. W. Hohmann, "Studying the TEM response of a 3-D conductor at a geological contact using the FDTD method". Geophysics, vol.60, no.4, pp.1265-1269, 1995.

[18] C. S. Chen, W. H. Chiu, and C. R. Lin, "Metal detection by multi-component TEM method". Terrestrial, Atmospheric and Oceanic Sciences, vol.20, no.3, pp.445-454, 2009.

[19] Z. Z. Xi, J. Liu, X. Long, et al., "Three-component measurement in transient electromagnetic method". Journal of Central South University (Science and Technology), vol.41, no.1, pp.272-276, 2010.

[20] A. A. Kaufman, and G. V. Keller, Frequency and transient soundings. Elsevier Science Ltd, 1983.

[21] S. Li, H. Sun, X. Lu, et al., "Three-dimensional modeling of transient electromagnetic responses of water-bearing structures in front of a tunnel face". Journal of Environmental and Engineering Geophysics, vol.19, no.1, pp.13-32, 2014.

[22] U. M. Kuzuoglu, R. Mittra, "Frequency dependence of the constitutive parameters of causal perfectly matched anisotropic absorbers". Microwave and Guided Wave Letters, IEEE, vol.6, no.12, pp.447-449, 1996.

[23] J. A. Roden, S. D. Gedney, "Convolutional PML (CPML): An efficient FDTD implementation of the CFS-PML for arbitrary media". Microwave and optical technology letters, vol.27, no.5, pp.334-338, 2000.

[24] M. N. Nabighian (Ed.), Electromagnetic Methods in Applied Geophysics Volume 1 – Theory. Society of Exploration Geophysicists, Tulsa, 1987.